Modified cure cycles for increased fatigue performance of fiber metal laminates

Johannes Wiedemann [a],[1],[*], Selim Mrzljak [b],[1], Josef Koord [c], Christian Hühne [a],[c], Frank Walther [b]

[a] *Technische Universität Braunschweig, Institute of Mechanics and Adaptronics, Langer Kamp 6, Braunschweig, 38106, Germany*
[b] *TU Dortmund University, Chair of Materials Test Engineering (WPT), Baroper Str. 303, Dortmund, 44227, Germany*
[c] *German Aerospace Center (DLR), Institute of Lightweight Systems, Lilienthalplatz 7, Braunschweig, 38108, Germany*

ARTICLE INFO

ABSTRACT

Modified (MOD) cure cycles that deviate from the manufacturer's recommended cure profile can reduce the inherent thermally induced residual stresses (TRS) in fiber metal laminates (FML). Literature shows that MOD cycles do not adversely affect the material properties but enhance the quasi-static material strength. However, the literature does not comprehensively discuss the impact of MOD cycles on material performance during cyclic fatigue loading. This paper, therefore, investigates how MOD cycles influence the fatigue characteristics of different FML layups made of carbon fiber-reinforced polymer (CFRP) and steel. The experimental results confirm that the quasi-static material strength and the modulus of the FML are increased when using MOD cure cycles. The evaluation of fatigue tests with digital image correlation, thermography, and electrical resistance measurements of notched specimens shows that a reduction of TRS delays damage initiation in the metal facesheets and decreases the crack growth rate until facesheet failure. The results further show that layup-dependent parameters, the maximum stress in the metal sheets, and metal sheet thickness significantly govern the evolution of fatigue damage. In summary, modified cure cycles are an efficient tool to enhance the quasi-static and fatigue performance of CFRP-steel hybrid laminates.

1. Introduction

Fiber metal laminates (FML), especially combinations of glass fiber-reinforced polymer and aluminum (GLARE), emerged from the motivation to improve the fatigue resistance of metallic aerospace materials [1]. The significantly enhanced resistance to fatigue crack growth and the higher fracture toughness led to the industrial application of GLARE in the Airbus A380 as a structural material for the upper fuselage panels.

Subsequently, further FML material combinations were studied, and application areas were demonstrated. By using high-modulus carbon fiber-reinforced polymer (CFRP) as opposed to glass fiber-reinforced polymer (GFRP) in GLARE, the overall FML stiffness can be substantially increased, which reduces the effective stress within the metal layers compared to GFRP-based laminates [2]. Moreover, using CFRP enables high residual load-bearing capabilities after metal failure due to the high strength of the carbon fibers [3]. In the high-cycle fatigue (HCF) regime, where the fibers can withstand the loads even after metal failure, significant increases in the lifetime of these FMLs are found [4,5]. The residual fatigue strength of the total laminate can be

twice as high as the life of the aluminum constituent. At the same time, with glass fiber reinforcement, only negligible differences are present for HCF.

In addition to substituting glass fibers with carbon fibers in the FML, the literature intensively discussed using other metals in combination with CFRP. The improvement of the fatigue performance of FML with CFRP has been shown in combination with, e.g. aluminum [5–7], titanium [8], magnesium [9,10] or steel [3,11,12]. The combination of CFRP and steel in an FML has advantages compared to combinations of CFRP with light alloy metals. The integration of steel enables quasi-static properties, which are unreachable with light metals [3]. Moreover, the bolt bearing strength of monolithic CFRP can be significantly increased by substituting CFRP layers with steel [11,13]. Also, repairing steel structures with one- or two-sided CFRP patches can delay crack initiation and decelerate crack growth. Depending on the CFRP stack thickness, improvements of up to 200% were found [12].

Given these findings, the increased resilience against crack growth makes CFRP ideal for FML. However, there are further aspects that need to be considered. One is the corrosion tendency between carbon

---

and metal [14] that must be controlled since it can reduce fatigue properties significantly [15]. Possible solutions prevent electrical conductivity through coating or using materials with suitable electrode potential. The other is the development of thermally induced residual stresses (TRS) during manufacturing due to the large difference in the coefficient of thermal expansion (CTE) between carbon fibers and metal and the high temperatures during manufacturing. Generally, these TRS lead to tensile stresses in the metal layers and compressive stresses in the fiber layers.

The amount of TRS is governed by the CTEs and stiffnesses of the FML constituents, the layup of the FML, and, on the other hand, by the cure cycle and the FML's temperature of operation [1,16,17]. The inherent stresses in the laminate reduce the theoretically possible strength of the combination of metal and fiber-reinforced polymer (FRP) to a certain extent [18]. Therefore, methods have been developed to reduce the unfavorable TRS state within an FML. For GLARE laminates, it was shown that a post-stretching step after manufacturing can reduce/reverse the unfavorable TRS state (tensile stresses in the metal layers and compressive stresses in the fiber layers) into a favorable state up to compression in the metal and tension in the fibers [1].

Khan et al. [19] showed that by reversing the TRS state in GLARE laminates, the residual compressive stresses in the metal layers lead to lower stress concentrations at a crack tip and, consequently, to extended fatigue life. Similar results were found for carbon fiber-reinforced aluminum laminates (CARALL) by Lin et al. [20], as well as for thermoplastic-based hybrid glass and carbon fiber-reinforced aluminum laminates [21]. For CFRP-steel laminates, Both [11] uses theoretical considerations to show a potential load increase of 79 % under cyclic loading if TRS are reversed by post-stretching of the laminate. The influence of post-stretching on the fatigue crack and delamination growth characteristics is also numerically described by Yeh [22] for aramid fiber-reinforced aluminum (ARALL).

However, during post-stretching, the favorable stress state is only applied in one direction, which is inconvenient for FML components designed for more than uniaxial loading conditions. Post-stretching is mainly applicable for planar structures, and it is difficult to assure a uniform stress distribution during post-stretching, leading to a significant variation in the TRS state [1]. For more complex GLARE specimens using stiffening doublers, Vlot et al. [23] revealed that post-stretching can even lead to increased fatigue delamination behavior, thus reducing fatigue life.

A more promising approach to changing TRS is using so-called smart or modified cure cycles that have been investigated for composites [24,25] and hybrid materials like FMLs [18,26]. In contrast to post-stretching, where the TRS is reversed, cure cycle modifications can only reduce the amount of TRS inside a composite laminate. Thus, the leverage of this method is much smaller. However, the method is applicable for more complex layups, part geometries, and loading conditions and, therefore, a promising tool to increase the performance of FML structures. Modified cure cycles are designed such that the point at which the individual layers of the laminate form a solid bond during manufacturing is shifted to the lowest temperature possible by adjusting the temperature profile during cure. This leads to significantly reduced internal pre-stresses in the laminate within the operating temperature range [24,26,27]. It was shown that reducing the TRS with modified cure cycles increases the quasi-static tensile strength of FRP [28] and FML [18,29].

Cure cycle modifications can even increase the interfacial lap-shear strength of FML [30], while also the shear strength of aramid-reinforced bonded joints [31] and the strength of adhesive joints under cryogenic temperatures [32] can be improved. Furthermore, modifying cure cycles can help to reduce the residual stress inhomogeneity in thick composite laminates [33] and decrease the distortions in multilayer composites [34]. Moreover, adjusting the temperature profile during the cure of thin-walled monolithic composite profiles can even influence the stability under axial compression [35–37].

The effect of the modified cycles and the corresponding reduced TRS on the fatigue behavior has been little studied. Kim et al. [28] investigated the influence of TRS on cross-ply 0°/90° FRP layups and showed that the fatigue life could be extended by reducing the TRS with modified cure cycles. An increase in fatigue life of up to 600 % is stated for low cycle fatigue (LCF). Kim et al. [38] show that a modified cure cycle can increase the torsional fatigue life of a hybrid aluminum/composite tube for high cycle fatigue. In contrast to [28], however, the influence gets small for load levels within the LCF regime. Khodja et al. [39] investigated the influence of cure cycle modifications on the fatigue performance of aluminum sheets with FRP repair patches. However, it remains unclear why increasing the curing time by 45 min at the recommended curing temperature of 120 °C shows the best fatigue results, although the highest component distortions indicate the highest TRS generated. Hausmann and Schmidt [40] applied an asymmetric cooling strategy in a hot press for asymmetric laminates (steel/CFRP) to reduce TRS and showed that a 10 % increase in cycles to failure in fatigue tests is achieved. Laliberté et al. [41] demonstrated that using modified cure cycles and consequently reduced TRS levels in GLARE laminates can shift fatigue initiation (defined as a 2 mm crack) towards higher numbers of cycles. However, a reduced fatigue initiation life for low TRS was observed for the highest load level tested. Whereas Ji et al. [8] reveal that the TRS state even determines the fatigue life after impact in thermoplastic CFRP-titanium laminates. Stress concentrations at the crack tip after impact are superimposed by the tensile residual stresses in the metal layers, which accelerates the propagation of fatigue cracks.

The literature review shows considerable interest in reducing TRS in FML to increase the performance of FML structures. Modifying the temperature profile during curing seems to be the most promising approach to reducing TRS. Most investigations focus on the influence of modified cure cycles on quasi-static properties, with little focus on their impact on fatigue behavior. Moreover, the literature focusing on fatigue behavior reveals some inconsistencies in experimental results and raises some questions.

Therefore, this work aims to comprehensively investigate the potential of reducing TRS with modified cure cycles to increase the fatigue life of FML on an experimental level. CFRP-steel laminates are chosen as a representative example of an FML with a wide range of possible applications and considerable thermally-induced residual stresses, and for which modified curing cycles have already been developed in the literature [26]. Different layups are investigated to consider various influencing variables and their effect on fatigue behavior. The FML layups differentiate in their laminate thickness, steel sheet thickness, metal volume fraction (MVF), number of interfaces (NoI), and facesheet thickness fraction (FTF). The TRS of the different FML layups are determined using asymmetric specimens and validated with X-ray diffraction measurements. The quasi-static tensile strength of the different layups is experimentally determined as a reference and for comparison with the literature. Subsequently, all the CFRP-steel layups are tested under tension/tension constant amplitude fatigue loading with two different maximum stress levels to characterize the influence of high and low TRS in combination with other layup-dependent variables on laminate fatigue. The experimental fatigue tests are monitored using three-dimensional digital image correlation cameras, high-speed thermography, and electrical resistance measurements.

2. Materials and methods

This section briefly overviews the materials and manufacturing processes, theoretical considerations about the stresses and strains evolving in the laminates due to the TRS and external loads, and the experimental testing methods used.

2.1. FML materials

The investigated FML in this work consists of a stainless steel alloy (X10CrNi18-8, DIN 1.4310, AISI 301) and a carbon fiber-reinforced

Table 1

Material properties for the CFRP-steel constituents. The index 1 indicates fiber direction (CFRP) and direction of rolling (steel), and index 2 denotes the transverse direction.

Value	Unit	Hexcel 8552-AS4	Steel 1.4310
E_1	GPa	122	191[b]
E_2	GPa	9.9	$E_1 = E_2$
G_{12}	GPa	5.2	73.5[c]
ν_{12}	–	0.27	0.3
t_{ply}	mm	0.13[a]	0.12/0.25
α_1	ppm/K	0.4 [49]	19.0 [17]
α_2	ppm/K	31.2 [49]	19.0

[a] Cured.

[b] Data from experimental tests.

[c] $G = \frac{E}{2(1+\nu)}$.

Table 2

Investigated FML layups and their characteristic parameters.

ID	Layup	t_{steel} [mm]	$t_{laminate}$ [mm]	MVF [%]	NoI [–]	FTF [%]
2	$[St/0°_4/St/0°_2]_S$	0.12	2.04	23.5	6	11.8
3a	$[(St/0°_4)_5/\overline{St}]_S$	0.12	6.52	20.2	20	3.7
4	$[(St/0°)_2/St/\overline{0°}]_S$	0.25	2.15	69.8	10	23.3
6b	$[(St/0°_4)_3/\overline{St}]_S$	0.25	4.87	35.9	12	10.3

t: thickness, MVF: metal volume fraction, NoI: number of interfaces, FTF: facesheet thickness fraction.

epoxy prepreg (Hexcel Hexply 8552-AS4). The material properties from the literature of these two constituents are given in Table 1. The material parameters partly differ when comparing different literature sources. In a previous investigation by Barth et al. [42], the values from Johnston [43] showed to be closest during structural dynamic investigations on an analytical and experimental level. They will, therefore, be also used in this work. In other previous works by Wiedemann et al. [17,44], slightly different material values were reported based on various literature sources. In [42], a detailed comparison between the different literature sources [43,45–48] is given. The biggest deviations are found in the elastic modulus in the fiber direction, which ranges from 122 GPa [43] to 141 GPa [46]. In the context of this work, however, the same conclusions can be drawn for any set of material parameters found in the literature for the two material constituents. The elastic modulus for the steel was determined in previous experimental tests for the steel sheet with a thickness of 0.12 mm. During these tests, a slight variation was observed between the values in the rolling (187 GPa) and transverse (194 GPa) directions of the steel sheets (cf. [44]). Since the deviations are small (below 5 %), an isotropic material behavior with the mean value is assumed in the context of this work. Identical material properties are considered for the thick steel sheets (0.25 mm).

2.2. Specimens and manufacturing

Numerous possibilities exist for FML layup variations. This work focuses mainly on the influence of the metal volume fraction (MVF), the laminate thickness, the number of interfaces (NoI) between metal and FRP, and the facesheet thickness fraction (FTF).

The two facesheets (outer layers) are steel for all layups, and all layups are symmetric in relation to the laminate center plane. All fiber plies are unidirectionally oriented to maximize the residual stress state in the laminates, which helps to emphasize the effect of the residual stresses on the other parameters under investigation. The fiber direction is equivalent to the rolling direction of the steel layers.

Hence, the metal volume fraction (MVF) is calculated from the quotient of metal to laminate volume:

$$\text{MVF} = \frac{V_{steel}}{V_{laminate}} \quad (1)$$

The number of interfaces (NoI) between metal and CFRP is defined by the number of steel layers in the laminate minus two:

$$\text{NoI} = \sum \text{steel layers} - 2 \quad (2)$$

The facesheet thickness fraction (FTF) is determined from the quotient of the facesheets' thickness to the laminate thickness:

$$\text{FTF} = \frac{2 \cdot t_{steel\ sheet}}{t_{laminate}} \quad (3)$$

To achieve a high variability within these four parameters, steel sheets of two different thicknesses (0.12 mm and 0.25 mm) are used. All these considerations result in the four layups in Table 2. With these
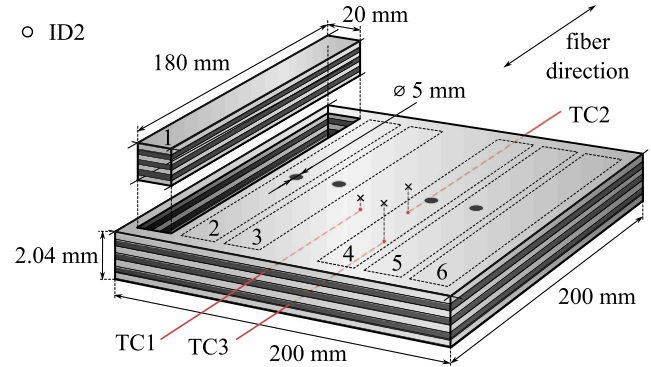

Fig. 1. Sketch of a specific laminate layup (ID2) from which the rectangular specimens are cut out via water jet cutting (layer thickness not to scale).

layups, a laminate thickness range of 2.04 mm to 6.52 mm, a range of the MVF of 20.2 % to 69.8 %, a range in the NoI of 6 to 20 and a range in the FTF of 3.7 % to 23.3 % is achieved.

The manufacturing process for all these laminates predominantly follows a classical process for manufacturing prepreg FRP materials, with an additional pre-treatment step for the steel material. Before the layup process, the steel sheets undergo mechanical treatment using a vacuum blasting process with corundum particles [50], followed by thorough cleaning to remove any dust particles using heptane. Subsequently, an aqueous sol–gel layer (AC-130-2) [51] is applied to the metal surface to ensure a robust interface between the metal and the FRP [52]. Following the sol–gel application, the metal sheets are immediately laminated with the prepreg layers and placed inside a vacuum bag before being transferred to an autoclave.

For each laminate configuration from Table 2 two plate like specimens with a size of 200 mm × 200 mm are manufactured, as shown in Fig. 1. Six rectangle-shaped specimens based on ISO 527-5 [53] type A, are cut out from each plate using water jet cutting. Due to the FML plate dimensions, the gauge length is reduced to 80 mm. While specimens 1 and 6 are tested for their quasi-static strength, specimens 2 to 5 are used during fatigue testing. After water jet cutting, a hole with a diameter of 5 mm (DH5) is drilled into the fatigue specimens.

The microsection of a manufactured laminate taken by light microscopy (Keyence VHX-5000) in Fig. 2 shows the prepreg consolidation and further illustrates the insignificant thickness of the sol–gel layer between the steel sheet and the neighboring CFRP plies.

To monitor the uniformity of the laminate temperature during cure, thermocouples (TCs) of type K were placed around the center of each plate specimen inside the laminate. The TCs were positioned at different heights in thickness direction within the CFRP layers to measure the temperature distribution inside the laminate during autoclave cure. The positions of the thermocouples for specimen ID2 are indicated in Fig. 1. A maximum of four TCs was used for specimens with layup ID3a. Additional thermocouples are placed on the bottom of the tool and on top of the vacuum bag within the autoclave.

The geometry of the fatigue specimens has a width-to-diameter (w/d) ratio of 4, which proved its usability in preliminary investigations [2,7] and was chosen based on realistic applications (e.g., rivet
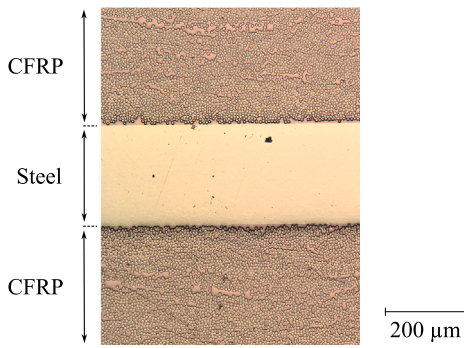
Fig. 2. Microsection of a manufactured laminate (light microscopy) shows the consolidated CFRP prepreg and the insignificant thickness of the sol–gel layer applied to the steel sheets.
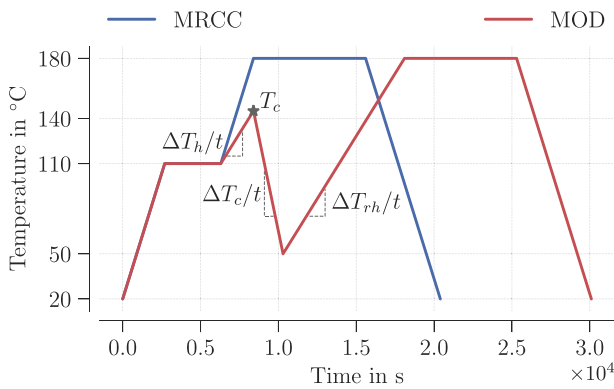

Fig. 3. Comparison of the manufacturer recommended cure cycle (MRCC) and a modified cure cycle (MOD) with an intermediate cooling step.

hole), and to keep material consumption in a reasonable range. Moreover, a w/d-ratio of 4 is still covered by analytical solutions for openhole tension of composite materials [54], which allows the correlation of the locations for crack initiation with analytical solutions. The tensile test specimens were chosen to have identical geometry as the fatigue test specimens except for the hole so that they can be cut from the same plate.

2.3. Cure cycles

The standard cure cycle for the prepreg material is illustrated in Fig. 3, labeled as the manufacturer-recommended cure cycle (MRCC). The MRCC involves a dwell stage at 110 °Celsius followed by a final curing stage at 180 °C before cooling down.

A modified cure cycle (MOD) tailored for the 8552-AS4 prepreg by Prussak et al. [26] is also presented in Fig. 3. This revised cure cycle incorporates a cooling step before the laminate is heated up to the final curing temperature, resulting in a lower temperature than the MRCC at which the individual plies of the laminate form a secure bond. As a result, this leads to decreased TRS within the laminate. The adjustment parameters are the temperature ramps during initial heating $\Delta T_h/t$, cooling $\Delta T_c/t$ and reheating $\Delta T_r h/t$ and the temperature T_c at which cooling is initiated in the process, as indicated in Fig. 3. Slightly adapted versions of this modified cure cycle have been demonstrated to significantly reduce TRS in laminates with layup ID2 in prior investigations [17,44].

Both cure cycles, MRCC and MOD, are employed for each layup (Table 2) in this study to produce specimens with identical layups but different TRS.

A homogeneous temperature distribution within the laminates during manufacturing and, hence, a homogeneous TRS state is necessary
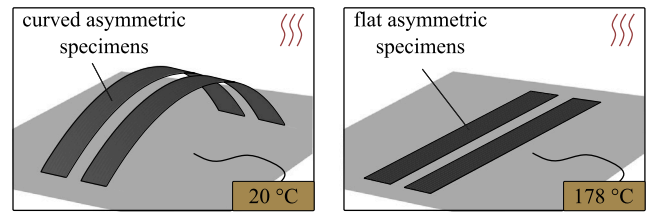

Fig. 4. Process to determine the stress-free temperature of asymmetric specimens inside a lab oven.

to directly correlate the fatigue test results to the TRS. As was shown in Prussak et al. [26], a temperature difference of 5 K when cooling is initiated or a difference in the heating or cooling ramps of 2 K min^{-1} can make a significant difference in the final TRS. It is assumed that the temperature measurement during the process is especially interesting for thick laminates or those possessing low thermal conductivity, equivalent to low metal volume fractions (ID3a). In aerospace applications, laminate thicknesses of up to 40 mm can be expected at, for example, the wing-root joints of upper and lower wing skins [55]. With increasing laminate thickness and lower MVFs, the heat flow into and out of the laminate decreases due to the low thermal conductivity of the polymer material. Hence, the assumption of a homogeneous TRS state within the entire laminate might not be valid anymore.

2.4. Analytical stress and strain quantification

This section presents the analytical correlations to quantify the ply-wise stresses in an FML by considering the superposition of external loads with internal residual stresses. Furthermore, the analytical solution to determine the strain field in a notched laminate is introduced.

2.4.1. Laminate ply stress

The laminate stresses in the FML layers are a superposition of thermally induced residual stresses and stresses evolving due to external loads.

To quantify the TRS within the laminates, an effective temperature difference ΔT is needed

$$\Delta T = T_r - T_{sf} \tag{4}$$

where T_r is the reference temperature at which the TRS are of interest and T_{sf} is the laminates' stress-free temperature. This temperature is defined by the laminate being free of any thermal stresses. Considering the case of pure linear thermo-elasticity and perfect instantaneous bonding of the single layers in the laminate, T_{sf} and the bonding temperature would be identical. In reality, however, non-linear effects like stress relaxation and the volumetric shrinkage of the resin or external process influences (e.g. tool material) can lead to differences between stress-free and bonding temperature [17].

The stress-free temperature is a parameter that is only sensitive to external influencing factors during the cure cycle but is independent of the layup [44]. Therefore, T_{sf} can be easily determined using asymmetric specimens within the manufacturing process of interest and is still valid for symmetric or other layup variations manufactured within the same process as long as the laminate temperatures are identical. The asymmetric specimens are manufactured on a flat tool but will start to curve upon demolding. Either the curvature can be evaluated to determine the stress-free temperature or, even more straightforward, they can be placed inside an oven and reheated until they reach their flat state again (cf. Fig. 4). The temperature prevailing in the flat state determines the stress-free temperature. Details on that method can be found in Wiedemann et al. [44].

Combining the TRS with any additional loads applied to a laminate, the effective stress $\sigma_{1,k}$ in the single layers of an FML can be calculated

with classical laminate theory (CLT). For details on the method, the reader is referred to e.g. Nettles [56]. First, the plane stress stiffness matrix $Q_{1,k}$ for each ply k needs to be calculated using the material parameters from Table 1

$$Q_{1,k} = \begin{bmatrix} \frac{E_1}{1-v_{12}v_{21}} & \frac{v_{12}E_2}{1-v_{12}v_{21}} & 0 \\ \frac{v_{12}E_2}{1-v_{12}v_{21}} & \frac{E_2}{1-v_{12}v_{21}} & 0 \\ 0 & 0 & G_{12} \end{bmatrix} \tag{5}$$

where in the following, the material coordinate system is denoted with indices 1, 2, 3, and the laminate coordinate system with x, y, z.

With the transformation matrix T

$$T = \begin{bmatrix} c^2 & s^2 & 2sc \\ s^2 & c^2 & -2sc \\ -sc & sc & c^2-s^2 \end{bmatrix} \tag{6}$$

where the terms s and c indicate $sin(\theta)$ and $cos(\theta)$, with θ being the ply angle in the laminate coordinates, the plane stress stiffness matrix can be transformed into the global coordinate system

$$\overline{Q}_k = T^{-1}Q_{1,k}(T^{-1})^T \tag{7}$$

With the coefficient of thermal expansion in the global coordinate system for each ply k

$$\alpha_{x,k} = T^T \alpha_{1,k} \tag{8}$$

and the ply coordinates z the equivalent thermal forces $N_{t,x}$ and moments $M_{t,x}$ per unit length can be calculated

$$N_{t,x} = \Delta T \sum_{k=1}^{n} \overline{Q}_k \alpha_{x,k}(z_k - z_{k-1}) \tag{9}$$

$$M_{t,x} = \frac{1}{2}\Delta T \sum_{k=1}^{n} \overline{Q}_k \alpha_{x,k}(z_k^2 - z_{k-1}^2) \tag{10}$$

Calculating the ABD matrices of the laminate

$$A_x = \sum_{k=1}^{n} \overline{Q}_k(z_k - z_{k-1}) \tag{11}$$

$$B_x = \frac{1}{2} \sum_{k=1}^{n} \overline{Q}_k(z_k^2 - z_{k-1}^2) \tag{12}$$

$$D_x = \frac{1}{3} \sum_{k=1}^{n} \overline{Q}_k(z_k^3 - z_{k-1}^3) \tag{13}$$

the midplane strains ε^0 and curvatures κ can be found

$$\begin{pmatrix} \varepsilon^0 \\ \kappa \end{pmatrix}_x = \begin{bmatrix} a & b \\ b^T & d \end{bmatrix}_x \left(\begin{pmatrix} N \\ M \end{pmatrix}_x + \begin{pmatrix} N_t \\ M_t \end{pmatrix}_x \right) \tag{14}$$

where a, b and d indicate the inverse of the entire matrix consisting of the ABD submatrices.

The total strain in global coordinate system $\varepsilon_{x,k}$ for each ply is consequently defined by

$$\varepsilon_{x,k} = \varepsilon_x^0 + z_k \kappa_x \tag{15}$$

and transforming that total strain into the material coordinate system for each ply

$$\varepsilon_{1,k} = (T^T)^{-1} \varepsilon_{x,k}, \tag{16}$$

the effective material strain $\varepsilon_{1,m,k}$, consisting of mechanical and thermal portion, is consequently calculated by subtracting the free thermal strain of the ply

$$\varepsilon_{1,m,k} = \varepsilon_{1,k} - \alpha_{1,k} \Delta T \tag{17}$$

and ultimately the effective ply stress $\sigma_{1,k}$ in the material system is calculated

$$\sigma_{1,k} = Q_{1,k} \varepsilon_{1,m,k} \tag{18}$$

In addition to evaluating the cure cycle-specific stress-free temperatures using asymmetric specimens, this work investigates whether
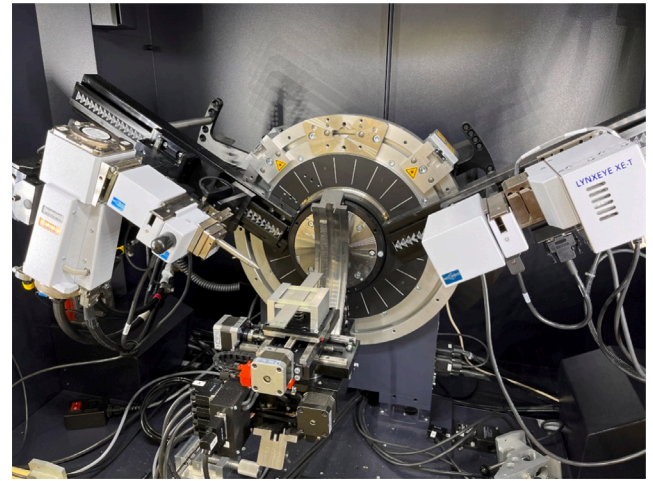

Fig. 5. Bruker D8 Discover X-ray diffraction measurement setup to determine the residual stresses in an FML using surface measurements.

Table 3
Hardware specifications for the X-ray diffraction measurements.

Parameter	Unit	Value
Target	–	Cr
Wavelength $k_{\alpha1}$	Å	2.2897
Bragg angle	°	128.8
Diffrac. plane $\{hkl\}$	–	Fe-γ $\{220\}$
Current	mA	40
Voltage	kV	30
Goniometer tilt	–	χ
Elastic modulus	GPa	191
Poisson ratio	–	0.3
Collimator diameter	mm	2
Ψ-Angle	°	(0; 11.25; 22.5; 37.25; 45)
Φ-Angle	°	(90; 270)

the TRS state in such an FML can also be determined using X-ray diffraction (XRD) measurements [57] within the austenitic stainless steel facesheets of the laminate. Using a Bruker D8 Discover XRD (Bruker, Billerica, USA) measurement setup (Fig. 5), the TRS in the top layer of each FML specimen are determined within a calculated depth of 12 μm. The hardware specifications for XRD setup can be found in Table 3. The experiments were carried out in the $sin^2 \Psi$-method, using Side-Inclination (χ-tilt of the goniometer). The surface residual stresses in the steel layers were measured before lamination and recorded as a reference. The reference was subsequently subtracted from the measurements of the laminates to obtain the TRS generated exclusively during the manufacturing process of the FML.

2.4.2. Strain field in notched laminates

Exact analytical solutions based on the Lekhnitskii formalism [58] are employed to determine the 2D deformations in an orthotropic elastic plate with a circular center notch loaded in tension. The derivation of the Lekhniskii formalism is frequently covered in literature [59–61]. The method's accuracy has been previously demonstrated by comparison to numerical and experimental (digital image correlation during testing) strain data in an OHT specimen [54]. In essence, the method combines the fundamental equilibrium equation for a 2D plate

$$\left. \begin{aligned} \frac{\partial \sigma_x}{\partial x} + \frac{\partial \tau_{xy}}{\partial y} + X = 0 \\ \frac{\partial \sigma_y}{\partial y} + \frac{\partial \tau_{xy}}{\partial x} + Y = 0 \end{aligned} \right\} \tag{19}$$

with the compatibility condition that ensures integrity and continuity during deformation

$$\frac{\partial^2 \varepsilon_x}{\partial y^2} + \frac{\partial^2 \varepsilon_y}{\partial x^2} - \frac{\partial^2 \gamma_{xy}}{\partial x \partial y} = 0 \tag{20}$$

Eq. (19) and Eq. (20) are connected through Hooke's law with the laminate compliance matrix $\mathbf{C}$ and the stress and strain vectors $\boldsymbol{\sigma}$ and $\boldsymbol{\varepsilon}$.

$$\boldsymbol{\sigma} = \mathbf{C}\boldsymbol{\varepsilon} \tag{21}$$

Combining these equations and introducing stress functions $\phi(z_1)$ and $\psi(z_2)$ yields following relation for determining the stresses in a 2D orthotropic plate

$$\begin{aligned}
\sigma_x &= 2\mathrm{Re}[\mu_1^2 \phi'(z_1) + \mu_2^2 \psi'(z_2)] \\
\sigma_y &= 2\mathrm{Re}[\phi'(z_1) + \psi'(z_2)] \\
\tau_{xy} &= -2\mathrm{Re}[\mu_1 \phi'(z_1) + \mu_2 \psi'(z_2)]
\end{aligned} \tag{22}$$

The expressions in Eq. (22) reduce the initial task of determining the stress distribution in an anisotropic 2D plate to finding expressions for the stress functions $\phi(z_1)$ and $\psi(z_2)$. Soutis and Filiou [61] present a closed-form exact analytical solution for the case of an open hole orthotropic plate under bi-axial loading. They introduce a loading ratio λ that defines the relation between the forces acting on the plate along the principal axes. Since the present paper considers an uniaxially loaded specimen with a circular center notch (OHT), λ is set to zero. The detailed formulation for the stress calculation is provided in Appendix. After determining the stresses in an OHT specimen, CLT is used to transform the results into strains, to allow for a comparison to DIC data.

2.5. Experimental testing

This section introduces the experimental setups used for quantifying the quasi-static and fatigue performance of the manufactured FMLs.

2.5.1. Quasi-static testing

For each layup and cure cycle, quasi-static tensile tests are performed on two FML specimens. For the tensile tests, an Instron 8802 (Instron, High Wycombe, UK) servo-hydraulic testing system with a load capacity of 250 kN is used in combination with an Instron dynamic extensometer (CAT No. 2620-603 with 10 mm gauge length, ± 1 mm travel) to record strain. The testing speed was set to 1 mm min^{-1}, suitable for the reduced measuring length.

2.5.2. Fatigue testing

The fatigue tests are performed with a Shimadzu EHF-EV50 (Shimadzu Corporation, Kyoto, Japan) servo-hydraulic testing system with a load capacity of 50 kN. During the tests, a 3D digital image correlation (DIC) system (Limess Q400 3D-DIC, Limess Messtechnik und Software GmbH, Krefeld, Germany) with 5 MP cameras is triggered at maximum stress to determine the crack length over time. Four cameras are used: two in the front (Ricoh TV lens FL-CC7528-2M, 75 mm focal length, 10 mm extension tube) and two in the rear (Ricoh TV lens FL-CC7528-2M, 75 mm focal length). The DIC lighting consists of LED light sources made by the manufacturer of the DIC system. Two lamps with a size of 100 mm $\times$ 120 mm and a radiation angle of 15° continuously illuminate the specimen with monochromatic blue light at an output of 4 W with a light intensity of 60 cd.

The temperature of the specimens is monitored with an Infratec ImageIR 8800 (InfraTec GmbH Infrarotsensorik und Messtechnik, Dresden, Germany) thermographic camera. A high-precision Keithley (Tektronix Inc., Beaverton, USA) system, containing a 2601B source measure unit connected via R232 null modem cable to a 2182 A nanovoltmeter (Tektronix Inc., Beaverton, USA), records the electrical resistance of the front metal facesheet. The system was operated in
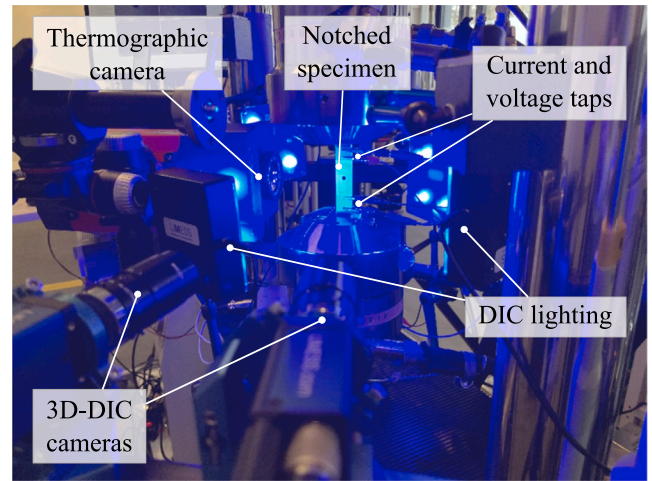

Fig. 6. Condition monitoring setup for fatigue testing: Servo-hydraulic testing system with front and rear instrumented DIC cameras, a thermographic camera oriented at the laminate edge, and current as well as voltage taps for electrical resistance measurement.

delta mode [7]. Electrical resistance measurements were performed to assess fatigue-related crack initiation and propagation. For reproducible measurement results, markers with a distance of 50 mm are added to the specimens to place the voltage drop clamps, and the current in/out clamps at identical locations for all specimens. Fig. 6 shows a photo of the measurement setup.

Constant amplitude tests (CATs) were conducted under ambient temperature with a sinusoidal load-time function at a stress ratio R = 0.1 (tension/tension loading). The laminates are tested under two different maximum stress levels (400 MPa and 600 MPa). One exception is the ID3a laminates, which were only tested for a maximum stress level of 400 MPa due to the load limit of the 50 kN testing machine.

The maximum stress levels were chosen based on the stress–strain data of the steel material. From previous experimental tests, a representative stress–strain curve for the steel sheet with a thickness of 0.12 mm is shown in green in Fig. 7. Linear elastic interpolation of the initial slope shows that the first plastification processes start from approx. 600 MPa. Both [11] has shown that a load far below the elastic limit does not lead to any damage mechanisms in fatigue tests up to 1×10^6 cycles in CFRP-steel laminates. In the regime of very high cycle fatigue (1×10^7 and higher), cracks can occur even at loads lower than the elastic limit, where special high-frequency fatigue testing systems are used for timely efficient characterization [21]. However, with regard to possible applications of the CFRP-steel laminate in this work, the focus is on the high cycle fatigue regime. Therefore, even though all the laminates have different stiffnesses due to their layup architecture, the two upper-stress levels of 400 MPa and 600 MPa are selected as a rough estimate. The stresses refer to the notched cross-section of the test specimens during the CAT. The testing frequency was set to 10 Hz for all experiments to avoid excessive testing time but also limit self-heating [3].

Besides evaluating the recordings of the thermographic and DIC camera images and the electrical resistance measurements, the force (F) and displacement (s) data of the testing machine, measured by load cell and linear variable differential transformer, is used to evaluate the specimen stiffness over its fatigue life. From stress–strain data of fatigue tests hysteresis values like the dynamic modulus E_{dyn} can be determined. E_{dyn} is an indicator for the damage accumulation with regard to the load cycle. Since the force–displacement data is used as the basis in this work, dynamic stiffness C_{dyn} is formulated instead of E_{dyn} as in [2,62]:

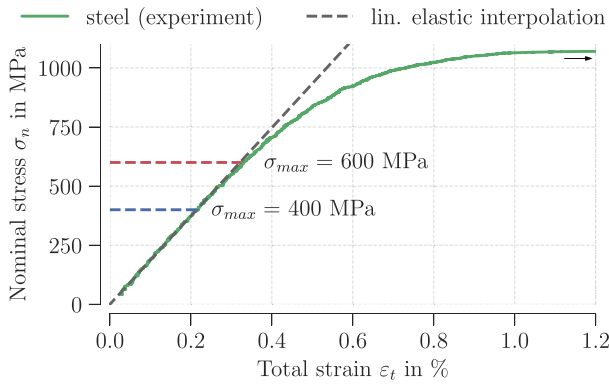$$C_{dyn} = \frac{F_{max} - F_{min}}{s_{max} - s_{min}} \tag{23}$$

Fig. 7. Definition of the two maximum stress levels σ_{max} for fatigue testing based on the experimental quasi-static stress–strain data of the steel sheet (thickness 0.12 mm).
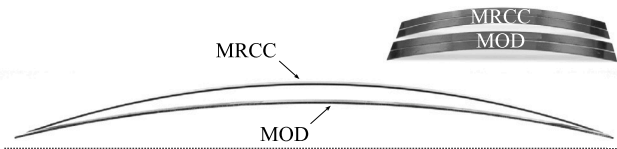

Fig. 8. Significant difference in the curvature at room temperature of asymmetric specimens manufactured with the two different cure cycles MRCC and MOD.

Table 4
Stress-free temperature evaluation for asymmetric specimens manufactured with the MRCC and MOD cycle.

Cycle	Mean [°C]	SD [°C]	RSD [%]	N
MRCC	178	0.5	0.3	8
MOD	136	3.2	2.4	5

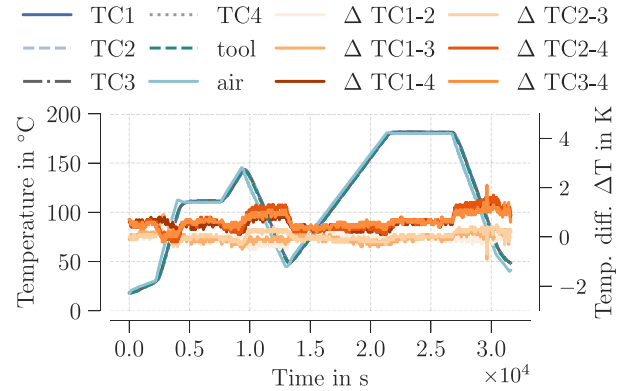(R)SD: (relative) standard deviation; N: number of specimens.

Fig. 9. Temperatures of all measurement positions during manufacturing of the specimen with layup ID3a using the modified cure cycle and resulting difference in the temperature readings between all the thermocouples placed inside the laminate at different positions in height.

For each resulting specimen configuration (layup, residual stress state, maximum stress level), one specimen is tested with extensive metrology applications to generate comprehensive data while limiting the testing time for an efficient testing routine.

3. Results

This section discusses the specimens' thermally induced residual stress states, including comparing the results from the asymmetric specimens with the XRD measurements and the temperature distribution during manufacturing. Subsequently, the results of the quasi-static tensile tests are shown. Finally, the fatigue test results are presented. These include the correlation of the specimens' surface strains with analytical solutions, the evolution of fatigue damage, and the influence of the TRS and other layup-dependent parameters on the fatigue performance of the investigated FML.

3.1. Modifying the thermally induced residual stress state

Fig. 8 shows a photo of asymmetric specimens manufactured with the MRCC and MOD cycles. A significantly smaller curvature for the specimens manufactured with the MOD cycle than those manufactured with the MRCC is visible.

Evaluating the stress-free temperatures for these specimens through reheating inside a lab oven (according to the procedure shown in Fig. 4) provides the data given in Table 4. The temperatures are determined from several specimens for each cycle. The table provides the standard deviations for each set of specimens. The specimens manufactured with the MRCC show a significantly smaller deviation of 0.5 °C compared to 3.2 °C for the specimens from the MOD cycle. However, the relative standard deviation for the MOD cycle is still only 2.4 %.

To ensure that the temperature inside the manufactured laminates is equally distributed throughout the curing process, the thermocouples placed inside the laminates at different positions in height are evaluated. The temperature measurements prove that the highest differences between the single temperature sensor positions are found within the specimens with layup ID3a (greatest thickness and smallest MVF) for

both cure cycles. Fig. 9 shows the monitored temperatures throughout the modified cure cycle for layup ID3a. The highest deviations between the single thermocouples inside the laminate can be found during the final cool-down for both cure cycles. However, at this stage in the curing process, the TRS state is already determined and will not be influenced anymore. When looking at the other curing stages in the process, the highest deviation is found to be 1.9 K for the MRCC just before reaching the maximum curing temperature of 180 °C. The highest deviation for the MOD cycle (excluding the final cooling stage) is found during the intermediate cooling step (1.3 K), as can be seen in Fig. 9. For the other layups, the deviations are even smaller. Compared to the 5 K difference discussed in [26], the difference measured in this work is assumed to be too small to result in significant deviations of the TRS across the laminate. Hence, the results show that the MOD cycle with its steep temperature ramps is still applicable for CFRP-steel with a thickness of 6.52 mm and an MVF of 20.2 %.

Considering the temperature measurements' results, the stress-free temperatures of the asymmetric specimens can be directly used to quantify the TRS of the plate specimens. With the values from Table 4 the TRS in laminate 1-direction (0°-direction) are calculated using CLT. The TRS in the fiber direction of the laminates is shown in Fig. 10 as a function of the metal volume fraction (MVF). The symbols indicate the four layups (cf. Table 2). The layup ID3a with the lowest MVF contains the highest tensile stresses in the metal sheets, whereas the specimens with layup ID4 (highest MVF) show the highest compressive stresses in the CFRP plies. With the MOD cycle, the TRS within the single layers of the laminate can be reduced by as much as 27 % for each layup compared to the specimens manufactured with the MRCC.

In Fig. 11, the TRS calculated with CLT and the cure cycle-specific stress-free temperatures from the asymmetric specimens are compared to the surface stress measurements using the XRD setup. It can be seen that the XRD values are all lower than the ones derived experimentally with asymmetric specimens. This is assumed to be due to a gradient of TRS from the sheet surface to the sheet inner, which, combined with the limited X-ray diffraction measurement depth, could lead to the measured lower values. Nevertheless, the X-ray diffraction measurements enable a fairly precise depiction of the relative TRS reduction (Table 5), with the advantage that the measurements can be carried out anywhere on the laminate surface without special preparation.
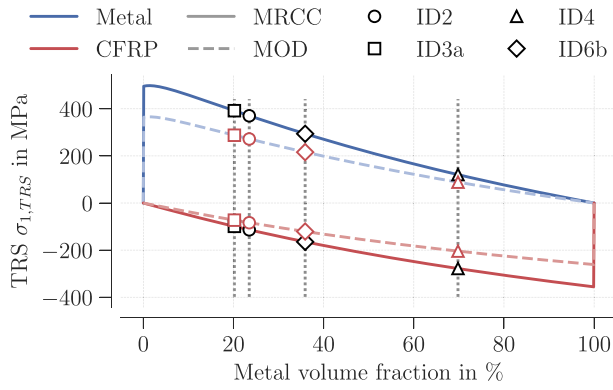
Fig. 10. Primary thermally induced residual stresses in 1-direction in the metal and CFRP layers of the FML as a function of the metal volume fraction and the cure cycle for a reference temperature T_r of 20 °C.
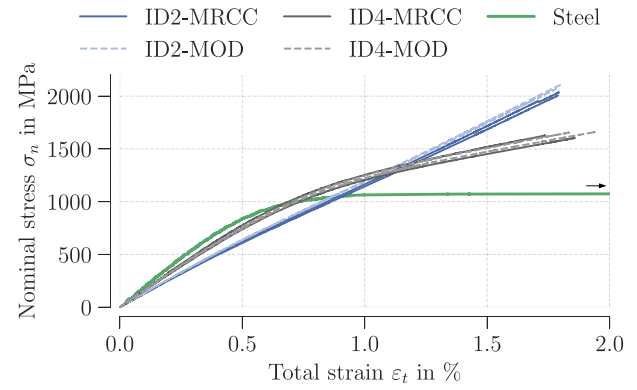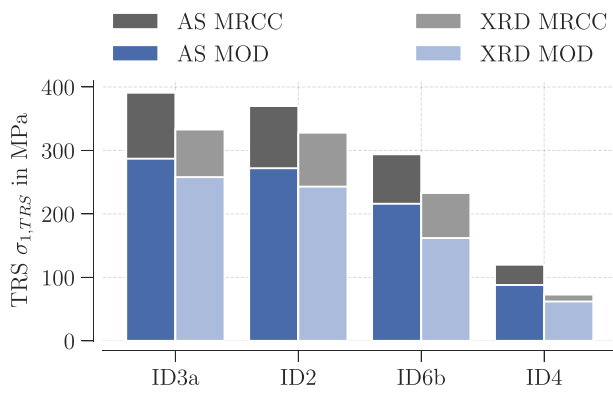

Fig. 11. Primary TRS in the steel sheets using the cure cycle-specific stress-free temperatures from asymmetric specimens (AS) and surface TRS in the top steel sheet based on X-ray diffraction measurements (XRD) for each layup and cure cycle ($T_r = 20$ °C).

Table 5
Comparison of measured relative TRS reduction due to modified cure using stress-free temperatures from asymmetric specimens (AS) and XRD measurements.

	ID2	ID3a	ID4	ID6b
AS	−27 %	−27 %	−27 %	−27 %
XRD	−26 %	−23 %	−15 %	−30 %

3.2. Quasi-static properties

Two FML specimens (cf. Fig. 1) are tested for their quasi-static strength for each layup and cure cycle. The specimens with ID3a could not be tested until final failure due to the high tensile forces needed. To show the influence of the MVF on the stress–strain behavior, Fig. 12 shows the stress–strain data for specimens ID2 (MVF: 23.5 %) and ID4 (MVF: 69.8 %). Additionally, the stress–strain data of the steel sheet (thickness 0.12 mm) is added as a reference. It is visible that with increasing MVF, the stress–strain curve better resembles the ductile behavior of the pure steel specimen. For lower MVF, the typical stress–strain behavior of CFRP is more evident in the data. The final failure of the FMLs occurs at approximately the same total strain for both layups, which is typical for FMLs in general, as the failure strain of the fibers governs ultimate laminate failure [1]. The results agree with investigations made in GLARE [41] regarding elastic modulus and ultimate strength. However, a decrease in failure strain for reduced TRS is not observed.

Furthermore, the results show that the modified cure cycle results in higher ultimate tensile strengths (UTS) of the specimens independent
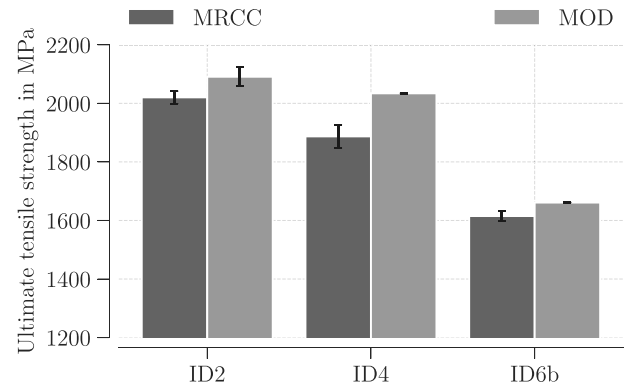

Fig. 12. Stress–strain curves from tensile tests for the ID2 and ID4 specimens. Tensile test results for the steel sheet (thickness: 0.12 mm) are given as a reference.

Fig. 13. Comparison of the ultimate tensile strength of specimens manufactured with different cure cycles (MRCC and MOD) and consequently different TRS.

Table 6
Evaluation of the ultimate tensile strength. Values of ID3a result from a linear interpolation of the stress–strain data from 0.75 % and an assumed ultimate failure strain of 1.75 %.

		ID2	ID3a	ID4	ID6b	
MRCC	Mean	2020	(2046)	1615	1887	MPa
	STD	21	(71)	17	40	MPa
MOD	Mean	2091	(2162)	1661	2034	MPa
	STD	32	(93)	0.5	1	MPa
	Delta	+3.5	(+5.7)	+2.8	+7.8	%

of the MVF. This is further illustrated in Fig. 13 for all specimens. A significant increase in the UTS is found for all specimens manufactured with the modified cure cycle. This is in good agreement with the literature [18,28,29]. More details can be found in Table 6. It is shown that a reduction of the TRS by around 27 % can increase the UTS by up to 7.8 %. If the absolute TRS reduction for the individual laminates is correlated with the laminate strength, a similar order of magnitude is found between relative TRS reduction and an increase in strength.

A similar picture can be found when evaluating the elastic modulus of the specimens tested in the quasi-static tests. The modulus evaluation is done in the strain range 0.05 % to 0.25 % according to ISO 527-5 [53]. Table 7 shows that an increase in modulus is found for the specimens where the TRS are significantly reduced using the modified cure cycle (ID2, ID3a, and ID6b).

3.3. Fatigue damage mechanism

Fig. 14 shows the verification of the 2D strain fields in the loading direction (ε_{xx}) of specimen ID6b at a stress level of 400 MPa. The

Table 7
Evaluation of the elastic modulus in the strain interval 0.05 % to 0.25 % (according to DIN EN ISO 527-5 [53]).

		ID2	ID3a	ID4	ID6b	
MRCC	Mean	127	129.5	159	137	GPa
	STD	1.70	4.53	7.57	0.42	GPa
MOD	Mean	131	136	157	138	GPa
	STD	0.14	2.97	1.91	1.91	GPa
	Delta	+3.0	+4.6	−1.3	+1.1	%
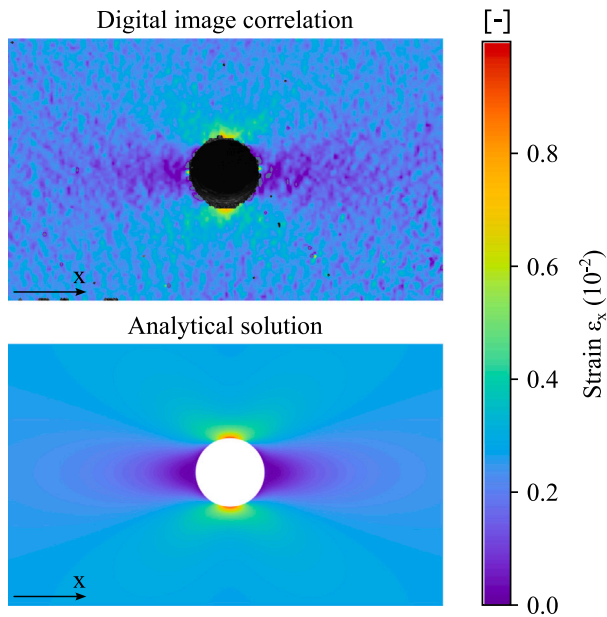
Fig. 14. Comparison of the strains in *x*-direction (specimen length direction) in the metal facesheet of layup ID6b (MRCC) from DIC (top) and analytical calculations (bottom) at a maximum stress σ_{max} of 400 MPa.

experimentally determined strain field through DIC measurement is compared to the analytically determined strain field around the center notch. It should be noted that the DIC results show the surface strain of the specimen, while the analytical result represents the midplane strain. However, due to the symmetry of the laminate and the fact that the specimen is not loaded in bending, the results are considered to be comparable.

The two strain fields are in excellent agreement. The shape of the strain descent from the concentration at the center towards the outer regions of the segment under consideration, and the peaks around the center hole are almost identical. This high level of agreement confirms the accuracy and validity of DIC measurement for further analysis of the structural behavior.

Considering the characteristics of the strain field, it is assumed that fatigue cracks are most likely to initiate at the strain concentration at the edge of the notch. While the strain field analysis allows for an assumption on the initiation point of cracking, the crack-growth behavior needs to be analyzed through testing.

During the fatigue tests, all specimens were tested up to a number of 6×10^5 cycles, except for the specimens ID4 that failed at around 1×10^5 ($\sigma_{max} = 400$ MPa) and 3×10^4 ($\sigma_{max} = 600$ MPa) cycles respectively. No final laminate failure occurred within 6×10^5 cycles for all other layups.

A similar failure damage pattern was found for all specimens independent of the layup and cure cycle. Images of the DIC cameras reveal the progression of the damage over the number of cycles during fatigue testing for the steel facesheets. Fig. 15 shows the strains in the loading direction (*x*-direction) on the ID6b specimen surfaces for specific load cycles. A crack is initiated in all facesheets at the stress concentration

point shown in Fig. 14. The crack propagates through the facesheet in the transverse direction until the complete metal sheet tears. It can be observed that the damage progresses simultaneously on the front and rear of the specimen. When comparing the two specimens with different TRS, damage progression for the specimen with reduced TRS is delayed. At 5.5×10^4 cycles, specimen ID6b MRCC experiences complete facesheet tear and considerable delaminations, whereas specimen ID6b MOD shows significantly less damage.

This difference in damage accumulation can also be found in the thermographic camera recordings. The thermographic camera is focused on one outer side of the specimen's laminate edge during the fatigue tests (cf. Fig. 6). Fig. 16 shows images of the two ID6b specimens (MRCC and MOD) for the same number of fatigue cycles. The laminate with higher TRS (top) exhibits a noticeably higher temperature at the same cycle count, indicating a more advanced state of damage progression. Furthermore, the image of the MRCC specimen reveals the failure of the inner steel plies after 5.5×10^5 cycles. Interestingly, multiple cracks occur per sheet within the inner steel sheets. This is due to the higher effective stress caused by the failed facesheets, leading to higher stress concentrations at the notch, also observed in [7]. In contrast, the MOD specimen does not show any cracks in the inner metal sheets, that have reached the outer specimen edge after the same number of cycles.

Evaluating the change in specimen temperature over the number of cycles shows that the temperature only increases when significant damage is present in the specimen. Fig. 17 shows the change in maximum temperature for the specimens with ID6b over the number of cycles. Additionally, the figure marks the number of cycles at which crack initiation and steel facesheet failure are detected. The results show that the inner steel sheet failure of specimen ID6b occurs well after the facesheet tear. A first increase in specimen temperature occurs just before the crack in the steel facesheet is initiated. After the failure of the facesheets, the specimen temperature stays relatively constant for the specimen with reduced TRS (ID6b MOD). In contrast, the temperature in the specimen with higher TRS further increases. This temperature increase indicates damage progression inside the laminate, accompanied by friction and consequent heat generation. This behavior is in accordance with the images shown in Fig. 16. The results demonstrate that thermal imaging can be used to monitor fatigue-induced damage in an FML. It can even detect the failure of layers inside the laminate by monitoring the specimen's temperature.

While Takamatsu et al. [63] showed that the crack lengths between the surface aluminum layer and the center aluminum layer are very similar, Burgers and Kempen [64] showed that there could also be a significant difference in crack length between facesheet cracks and cracks in the inner metal sheets. This is because the facesheets are only supported by bridging fibers from one side in contrast to the layers inside the laminate [65]. Based on the results, the damage evolution in the investigated CFRP-steel laminates is assumed to follow the latter damage mechanism.

Besides using the DIC images to identify facesheet crack initiation and failure, electrical resistance (ER) measurements are used. Since the electrical taps directly contact the facesheets of the specimens, facesheet damage leads to increased ER between the two taps attached to the top and bottom of a specimen. Fig. 18 shows the normalized ER of the specimen surface for layups ID3a and ID6b in comparison. Again, the cycle counts where crack initiation and facesheet failure occur, identified via DIC, are marked. It can be seen that the ER increases significantly when the facesheets tear half and entirely, as observed in [7]. Comparing the identical layups manufactured with the two different cure cycles, a delayed failure of the facesheet of the specimens with reduced TRS is observed for both layups, as was already found in the DIC images (cf. Fig. 15). When zooming into the data of the ER measurements (Fig. 19) an increase in ER can even be detected just after crack initiation in the facesheets. Hence, measuring ER is an
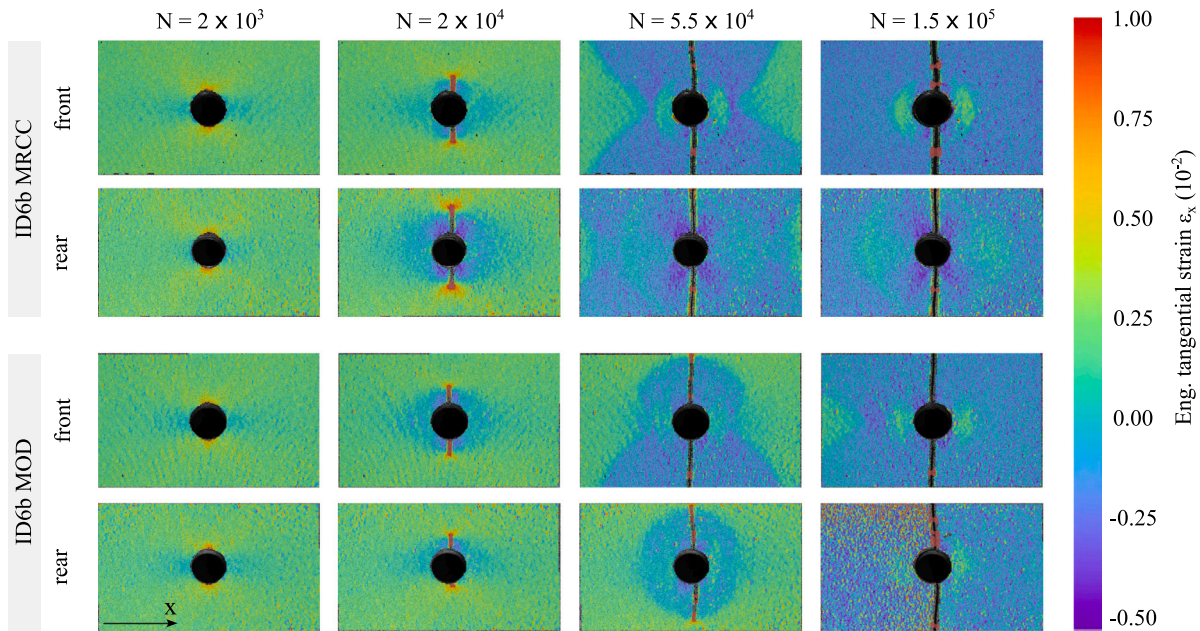
Fig. 15. Tangential strains ϵ_x (load direction) at maximum stress ($\sigma_{max} = 400$ MPa) on the front and rear surface of specimens with layup ID6b for selected numbers of cycles show the difference in damage progression for the two TRS states.
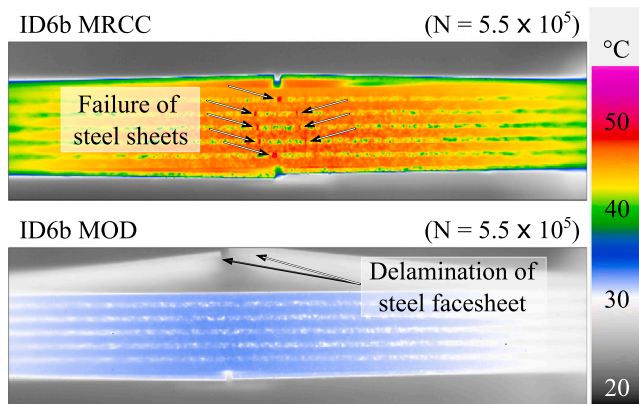

Fig. 16. Inner steel sheet failure can be observed in the thermographic camera recordings for ID6b MRCC after 5.5×10^5 cycles at maximum stress ($\sigma_{max} = 400$ MPa). For ID6b MOD, the specimen temperature is significantly lower, and no inner steel sheet failure is observed after the same number of fatigue cycles.

Fig. 18. Normalized electrical resistance of the steel facesheets during fatigue testing. Symbols indicate crack initiation and facesheet failure.

Fig. 17. Change in maximum specimen surface temperature for layup ID6b at a testing frequency of 10 Hz.

effective method for monitoring the state of damage in the facesheets of this investigated FML.

Therefore, DIC image data and ER measurements are evaluated to define the cycle number at which crack initiation and facesheet failure within all laminates tested. Crack initiation is determined by the cycle with a significant increase in ER and a significant change in the strain peak extending into the crack propagation direction. The facesheet failure is defined by the gradient of the ER approaching infinity and the cracks being extended towards the outer edges on both the front and rear of the specimens.

The evaluation of the dynamic stiffness, defined in Eq. (23), provides further insights into damage progression in addition to looking at the imaging techniques and ER measurements. Fig. 20 shows the force–displacement data for selected numbers of cycles beginning with $N = 2 \times 10^3$ up to $N = 5.5 \times 10^5$ for ID2 specimens. For both specimens (MRCC and MOD), a decrease in dynamic stiffness for an increasing number of cycles is observed. However, for the MRCC specimen, this effect is more pronounced, especially towards higher numbers of cycles. This indicates more significant damage after the same number of cycles, which is in accordance with the thermal imaging data (cf. Fig. 16). While both specimens exhibit creep, indicated by the horizontal shift of
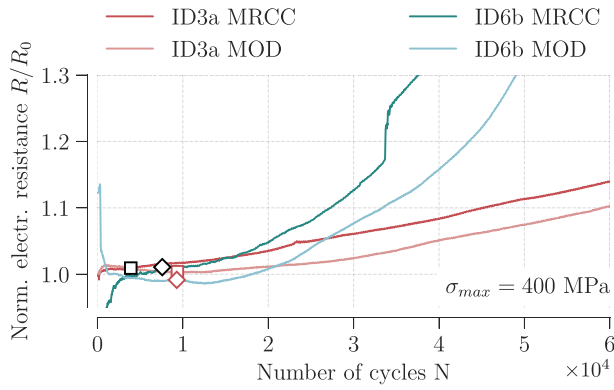
Fig. 19. A magnification shows a clear increase in normalized electrical resistance shortly after the crack initiation in the steel facesheets for all specimens.
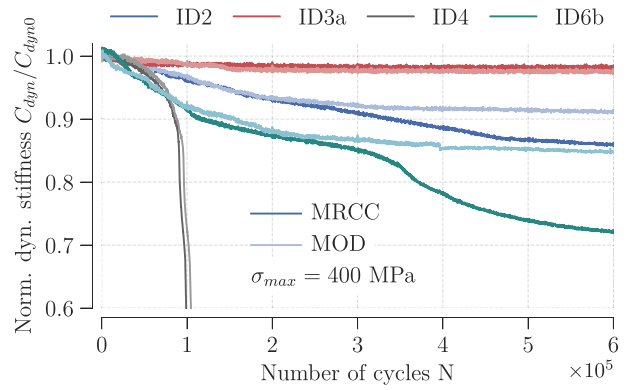

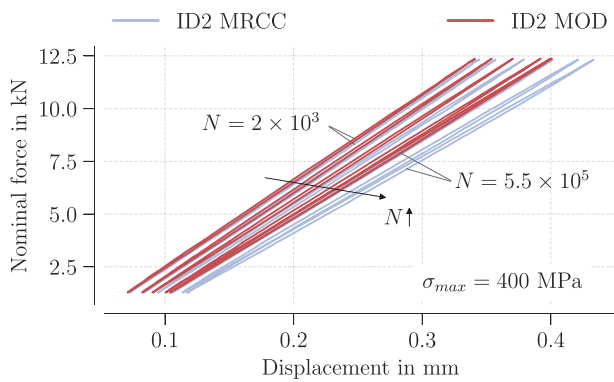**Fig. 21.** Normalized dynamic stiffness over the number of cycles for all tested layups and TRS and a maximum stress σ_{max} of MPa.

Fig. 20. Load hysteresis for selected numbers of cycles N (2×10^3, 2×10^4, 1×10^5, 2.5×10^5, 4×10^5, 5.5×10^5) show a more prominent decrease in dynamic stiffness and advanced creep state for ID2 MRCC with increasing number of cycles compared to ID2 MOD.

Fig. 22. Numbers of cycles for facesheet crack initiation, facesheet failure, and specimen failure correlated with the metal volume fraction.

3.4. Parameters determining the fatigue performance

the load hysteresis for an increasing number of cycles, the MRCC specimen shows accelerated and increased creep due to higher temperature and advanced damage propagation.

The dynamic stiffness over the number of cycles is derived for all laminates tested. In Fig. 21, the dynamic stiffness is normalized on the initial dynamic stiffness of each specimen and plotted for all layups. The results refer to the tests performed with a maximum stress σ_{max} of 400 MPa. Different behavior is observed for the different layups. Specimens of ID3a show a relatively continuous dynamic stiffness up to 6×10^5 cycles. Specimens ID2 and ID6b show significant decreases in the dynamic stiffness, which can be attributed to the progressing damage inside the laminate. For both layups, the specimens with higher TRS show a more pronounced decrease in dynamic stiffness for higher load cycles. Again, this indicates internal damage progression, as seen in the thermographic camera images in Fig. 16 and the temperature evolution in Fig. 17. For layup ID4, an early total laminate failure is observed for both TRS states. It is plausible that both specimens with differing TRS states show similar fatigue characteristics as the difference in the TRS state of layup ID4 is small (cf. Fig. 11).

All the data shows that the specimens manufactured with the modified cure cycle appear more tolerant to fatigue. Cracks in the facesheets are initiated with a delay, the crack growth is slower, and the residual strength and stiffness after facesheet failure increase. This is especially true for the laminates ID2, ID3a and ID6b. For layup ID4 complete laminate failure occurs soon after facesheet tear.
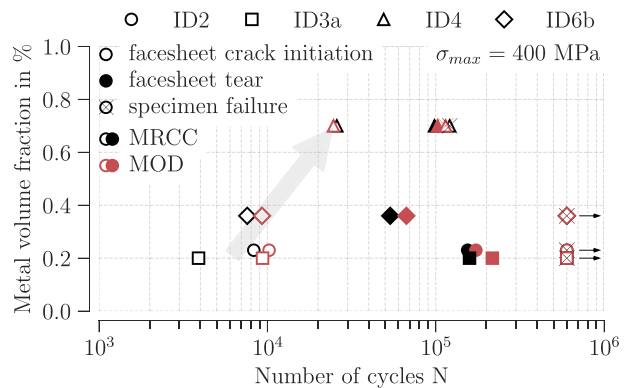
Determining the fatigue damage mechanism using the presented methods shows significant differences between the different layups and thermally induced residual stress states investigated. The results for various influencing variables are presented below to attribute the different behaviors to individual parameters. For this purpose, the cycle count for the significant events describing the damage progression in the laminates is used. This way, correlations between the parameters and damage can be revealed. The events are the crack initiation in the facesheets of the laminates and the failure (tear) of the facesheets. Laminate failure is not considered since it only occurred for layups ID4 for the number of cycles tested.

The metal volume fraction is the first relevant parameter considered from Table 2. Fig. 22 shows the fatigue damage events and their corresponding cycle count for each layup and TRS state against the corresponding metal volume fraction. It can be seen that the crack initiation in the facesheets occurs before 1×10^4 cycles for all layups except for ID4. Furthermore, for identical layups, the crack initiation for MRCC specimens always starts before the crack initiation within specimens manufactured with MOD. This effect is more pronounced for the specimens with high TRS in the metal sheets (ID2, ID3a, and ID6b). For specimens with layup ID4, with low TRS in the metal sheets, there is no significant difference in time for the occurrence of cracks in the facesheets.

The results suggest a correlation between crack initiation and the metal volume fraction. The initiation of cracks around the notch is delayed for higher metal volume fractions and, consequently, lower tensile TRS in the metal sheets. This correlation is indicated by the
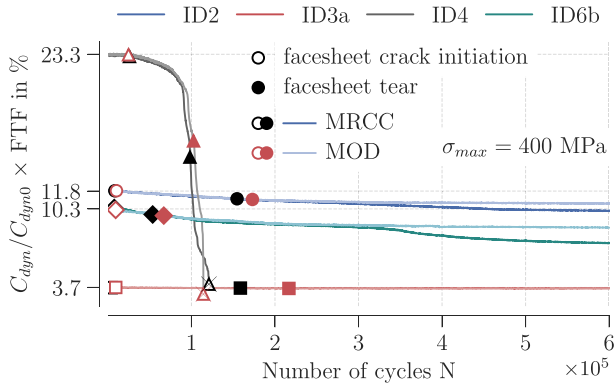
Fig. 23. The dynamic stiffness decreases much faster after failure of the facesheets with increasing facesheet thickness fraction (FTF).

Fig. 24. Increase in number of cycles between steel facesheet crack initiation ($N_{c.i.}$) and tear (N_t) using the MOD cycle in contrast to the MRCC for the two different maximum stress levels tested.

arrow in Fig. 22. However, the tear of the facesheets does not seem to be correlated with the metal volume fraction.

The second parameter in Table 2 that distinguishes the different types of layups is the number of interfaces between CFRP and metal. However, no correlation between the number of interfaces and the cycle count was found regarding crack initiation or facesheet tear.

The third parameter is the facesheet thickness fraction (FTF). Fig. 23 correlates the normalized dynamic stiffness and FTF against the number of cycles when significant damage events occur. The results show that for high FTF (ID4), the crack initiation in the facesheets results in a substantial decrease in the dynamic stiffness of the laminate. For lower FTFs, the influence is less pronounced. For specimens ID2 and ID6b, the dynamic stiffness continuously decreases with increasing damage accumulation in the facesheets. An additional drop in stiffness is observed significantly after facesheet tear, which can be attributed to the failure of the inner metal sheets based on the thermographic images. Meanwhile, for low FTF (ID3a), no significant change in dynamic stiffness is observed even after facesheet tear. Since the facesheets fail first in the investigated laminates, the proportion of the facesheets in the overall composite is decisive for the amount of dynamic stiffness reduction after the tear and failure of the facesheets.

The investigations show that the layup-dependent parameters, metal volume fraction, and face sheet thickness fraction significantly influence the fatigue characteristics. In contrast, the number of interfaces does not correlate with the damage behavior.

The influence of the modified cure cycles on the fatigue performance of the laminates is best illustrated by the crack growth rate in the metal sheets. The number of cycles between facesheet crack initiation $N_{c.i}$ and facesheet tear N_t is used to evaluate the crack growth rate. Fig. 24 shows the increase in cycles between crack initiation and tear of the facesheets when using the MOD cycle in contrast to the MRCC. An increase in cycles can be found for all investigated laminates and tested stress levels. This behavior can be attributed to reduced stress peaks at the crack tip due to lower TRS in the metal sheets. An effect that is comparable to what is found for post-stretched laminates [19]. However, it is assumed that the extent is greater for post-stretched laminates due to the reversed TRS state inside the laminate (compression within the metal sheets). Moreover, the results show for a fatigue stress level of 400 MPa that the influence of the reduced TRS on the crack growth depends on the absolute TRS state in the laminates. The increase in cycles between $N_{c.i}$ and N_t is greater for laminates with high TRS. The results generated with a fatigue stress level of 600 MPa indicate a contradictory behavior but still show a significant decrease in crack growth for the laminates with reduced TRS.

To correlate the maximum stresses in the metal sheets with the events detected during fatigue testing, the maximum effective stress in the metal sheets is calculated for each tested specimen according
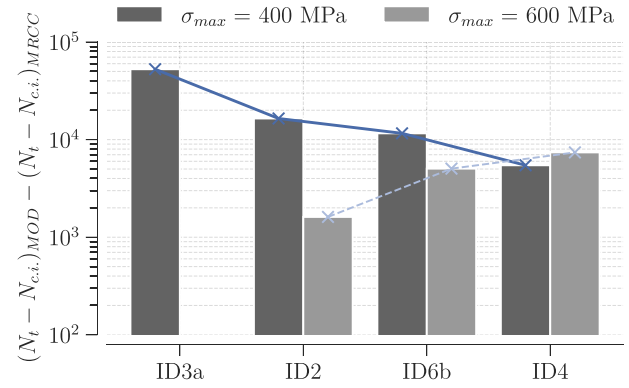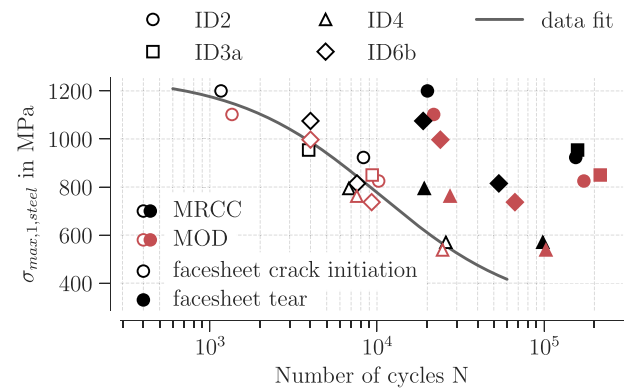

Fig. 25. The experimental data indicates a direct correlation between crack initiation and the maximum stress in the metal sheets for all investigated layups and stress levels.

to Eq. (18). The maximum stress is a superposition of the TRS with the externally applied forces during testing. Fig. 25 shows the numbers of cycles for crack initiation and facesheet tear dependent on the maximum stress in the metal sheets for each tested configuration. Four data points are plotted for each layup: two TRS states and two maximum stress levels in the test (except for layup ID3a). The results show a strong correlation between the maximum stress in the steel sheets $\sigma_{max, 1, steel}$ in loading direction and the numbers of cycles for crack initiation $N_{c.i.}$ for all laminates. To illustrate this correlation, a function is fitted through the experimental data

$$\sigma_{max, 1, steel} = \frac{a}{b + N_{c.i.}} + c \tag{24}$$

where a, b, and c are the fitting parameters.

A comparable correlation between maximum stress in the metal sheets and facesheet tear cannot be found in Fig. 25. In contrast, the number of cycles between crack initiation and facesheet tear ($N_t - N_{c.i.}$) seems to correlate with the normalized stress ratio derived from maximum stress in the metal sheets $\sigma_{max, 1, steel}$ and ultimate laminate strength $\sigma_{ult, lam}$:

$$\frac{\sigma_{max, 1, steel}}{\sigma_{ult, 1, lam}} = \frac{a}{b + (N_t - N_{c.i.})} + c \tag{25}$$

The normalized stress ratio to evaluate fatigue behavior was also used, e.g., in [66]. Fig. 26 shows the respective number of cycles against the normalized stress ratio for all layups tested. Significant differences between the layups with different metal sheet thicknesses can be found. For layups with thin steel sheets (ID2 and ID3a, steel sheet thickness: 0.12 mm) significantly higher numbers of cycles between facesheet crack initiation and tear are found for the same normalized
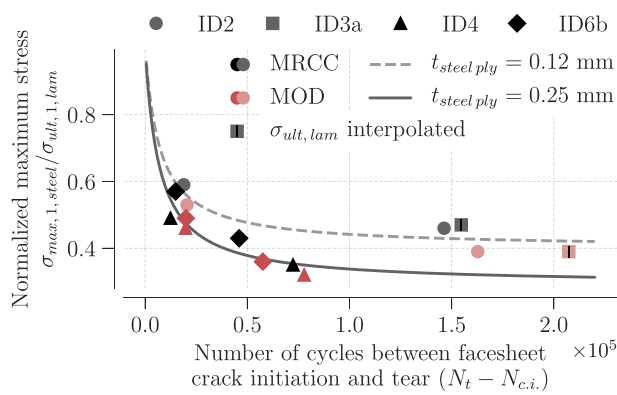
Fig. 26. The experimental results indicate a difference in damage evolution between layups with thin (ID2 and ID3a) and thick (ID4 and ID6b) metal sheets.

maximum stress. Whereas layups with thick steel sheets (0.25 mm) show accelerated crack growth. The function presented in Eq. (25) is fitted independently for the layups with differing steel sheet thicknesses (ID2/3a and ID4/6b). It is assumed that the thinner steel sheets (0.12 mm) allow a better fiber bridging mechanism compared to the thicker sheets (0.25 mm). Therefore, the crack propagation rate in the metal facesheets is significantly slowed after crack initiation.

4. Conclusion

Modified cure cycles can significantly reduce the thermally induced residual stresses in an FML. The curvature and stress-free temperature evaluation of asymmetric laminates confirm this. Moreover, X-ray diffraction measurements on the metal surface of the investigated FMLs show the same amount of relative stress reduction.

Although the TRS reduction is smaller compared to, for example, post-stretching processes, the TRS level significantly influences the quasi-static properties of the FML. Both ultimate strength and elastic modulus increase for reduced TRS levels when laminates have high metal volume fractions.

The agreement of digital image correlation (DIC) deformation data during fatigue testing with analytically calculated strain fields shows that damage is initiated in notched specimens at positions with high stress concentrations. Early damage initiation and preliminary facesheet failure are observed in specimens with higher TRS than those with reduced TRS. The electrical resistance measurements confirm these observations. Thermographic imaging detects the facesheet failure and, remarkably, damage inside the laminate due to increased friction at damaged interfaces. Similarly to the effects seen from the outside (using DIC), internal damage is observed earlier within specimens with high TRS. The different methods to monitor damage progression and specimen failure complement each other well, providing a comprehensive picture of the damage mechanisms.

Experimental fatigue test results show that the metal volume and facesheet thickness fraction significantly determine the damage evolution from the parameters defined by the laminate layup. In contrast, the number of interfaces between metal and fiber layers inside the FML shows no significant influence.

The reduction of TRS with modified cure cycles improves the fatigue performance for all investigated laminate configurations. On the one hand, the reduced TRS reduces the maximum stress in the metal sheets, leading to delayed crack initiation. On the other hand, the reduced TRS also slows the crack growth, leading to an increase in cycles of 1×10^3 to 5×10^4 from crack initiation until facesheet failure, depending on the layup and fatigue loading level. Furthermore, the results indicate that the crack growth rate depends on the thickness of the steel sheets within the FML. Besides the damage initiation, even after the facesheets

fail, the TRS reduction leads to a more damage-tolerant behavior. The dynamic stiffness decrease after facesheet failure is less pronounced than for the laminate counterparts with high TRS. The inner layers of the laminate seem to possess a higher load reserve after the failure of the facesheets when the TRS is reduced.

The results show that the TRS significantly influences the quasi-static and fatigue performance of the tested CFRP-steel laminates. No adverse effect on the mechanical performance of the laminates could be observed for the tested laminates. Therefore, reducing TRS with modified cure cycles efficiently increases FML capability without compromising other performance parameters.

In future work, X-ray diffraction for TRS determination seems promising. It enables local determination of the TRS state without applying measurement necessities like strain gauges. Moreover, the evolution of TRS during fatigue testing can be monitored. The absolute influence of the TRS on the quasi-static and fatigue characteristics must be statistically confirmed. Furthermore, the results must be validated for additional load levels and under variable amplitude tests, including tension/compression, and for more laminate layups. In particular, FMLs with facesheets made of the fiber constituent and laminates with more than a single fiber direction are of interest. Finally, future cyclic tests should focus on the final laminate failure to investigate the influence of the TRS and other parameters on the FML residual strength. The results will help to further optimize the curing process, especially for larger FML parts using quantified optimization procedures.

CRediT authorship contribution statement

Johannes Wiedemann: Writing – review & editing, Writing – original draft, Visualization, Validation, Methodology, Investigation, Formal analysis, Data curation, Conceptualization. **Selim Mrzljak:** Writing – review & editing, Writing – original draft, Visualization, Validation, Methodology, Investigation, Formal analysis, Data curation, Conceptualization. **Josef Koord:** Writing – review & editing, Writing – original draft, Formal analysis. **Christian Hühne:** Writing – review & editing, Resources, Project administration, Funding acquisition. **Frank Walther:** Writing – review & editing, Resources, Project administration, Funding acquisition.

Declaration of competing interest

The authors declare that they have no known competing financial interests or personal relationships that could have appeared to influence the work reported in this paper.

Acknowledgment

The authors would like to thank Mareike Stegmaier for her contribution to the manufacturing and preparation of the laminates for testing. The high quality of the laminates and the consistency of the production process are crucial factors for ensuring the validity of the results.

Funding

Appendix

The analytical solution proposed by Soutis and Filiou [61] is presented herein. Firstly, the complex parameters are defined:

$$\alpha_0 = \sqrt{\frac{E_{xx}}{E_{yy}}}, \quad \beta_0 = \frac{E_{xx}}{2G_{xy}} - \nu_{xy}$$

if $\beta_0 \geq \alpha_0$:

$$s_1 = i\left(\sqrt{\frac{\beta_0 - \alpha_0}{2}} + \sqrt{\frac{\alpha_0 + \beta_0}{2}}\right)$$

$$s_2 = i\left(-\sqrt{\frac{\beta_0 - \alpha_0}{2}} + \sqrt{\frac{\alpha_0 + \beta_0}{2}}\right)$$

if $\alpha_0 \geq \beta_0$:

$$s_1 = \sqrt{\frac{\alpha_0 - \beta_0}{2}} + i\sqrt{\frac{\alpha_0 + \beta_0}{2}}$$

$$s_2 = -\sqrt{\frac{\alpha_0 - \beta_0}{2}} + i\sqrt{\frac{\alpha_0 + \beta_0}{2}}$$

The real and imaginary parts of the complex parameters are then used in the following:

$$\alpha_i = \text{Re}(s_i), \beta_i = \text{Im}(s_i), i \in [1, 2]$$

The 2D stress field at any position in an orthotropic plate can be determined using:

$$\sigma_{xx} = p + \text{Re}\left\{\frac{p}{s_1 - s_2}\left[\frac{-is_1^2}{1 + is_1}\Omega_1 + \frac{is_2^2}{1 + is_2}\Omega_2\right]\right\}$$

$$\sigma_{yy} = \text{Re}\left\{\frac{p}{s_1 - s_2}\left[\frac{-i}{1 + is_1}\Omega_1 + \frac{i}{1 + is_2}\Omega_2\right]\right\}$$

$$\tau_{xy} = -\text{Re}\left\{\frac{p}{s_1 - s_2}\left[\frac{-is_1}{1 + is_1}\Omega_1 + \frac{is_2}{1 + is_2}\Omega_2\right]\right\}$$

with

$$\Omega_j = \left(1 - \frac{x + s_j y}{\sqrt{\left(x + s_j y\right)^2 - R^2\left(1 + s_j^2\right)}}\right), \quad j \in [1, 2]$$

Data availability

Data will be made available on request.

References

[1] Alderliesten R. Fatigue and fracture of fibre metal laminates. In: Solid mechanics and its applications, vol. 236, Cham: Springer; 2017.

[2] Trautmann M, Mrzljak S, Walther F, Wagner G. Mechanical properties of thermoplastic-based hybrid laminates with regard to layer structure and metal volume content. Metals 2020;10(11):1430. http://dx.doi.org/10.3390/met10111430.

[3] Mrzljak S, Schmidt S, Kohl A, Hülsbusch D, Hausmann J, Walther F. Testing procedure for fatigue characterization of steel-CFRP hybrid laminate considering material dependent self-heating. Materials (Basel, Switzerland) 2021;14(12). http://dx.doi.org/10.3390/ma14123394.

[4] Dadej K, Bieniaś J, Surowska B. Residual fatigue life of carbon fibre aluminium laminates. Int J Fatigue 2017;100:94–104. http://dx.doi.org/10.1016/j.ijfatigue.2017.03.026.

[5] Dadej K, Bieniaś J. On fatigue stress-cycle curves of carbon, glass and hybrid carbon/glass-reinforced fibre metal laminates. Int J Fatigue 2020;140:105843. http://dx.doi.org/10.1016/j.ijfatigue.2020.105843.

[6] Austin T, Singh MM, Gregson PJ, Powell PM. Characterisation of fatigue crack growth and related damage mechanisms in FRP–metal hybrid laminates. Compos Sci Technol 2008;68(6):1399–412. http://dx.doi.org/10.1016/j.compscitech.2007.11.013.

[7] Mrzljak S, Trautmann M, Blickling P, Wagner G, Walther F. Fatigue condition monitoring of notched thermoplastic-based hybrid fiber metal laminates using electrical resistance measurement and digital image correlation. J Compos Mater 2023;57(17):2669–87. http://dx.doi.org/10.1177/00219983231176257.

[8] Ji C, Hu J, Alderliesten R, Yang J, Zhou Z, Sun Y, et al. On the post-impact fatigue behavior and theoretical life prediction of CF/PEEK-titanium hybrid laminates using an energy dissipation approach. Compos Sci Technol 2024;245:110354. http://dx.doi.org/10.1016/j.compscitech.2023.110354.

[9] Zhou X, Zhao Y, Chen X, Liu Z, Li J, Fan Y. Fabrication and mechanical properties of novel CFRP/Mg alloy hybrid laminates with enhanced interface adhesion. Mater Des 2021;197:109251. http://dx.doi.org/10.1016/j.matdes.2020.109251.

[10] Pan Y, Wu G, Huang Z, Li M, Ji S, Zhang Z. Effect of surface roughness on interlaminar peel and shear strength of CFRP/Mg laminates. Int J Adhesion Adhesives 2017;79:1–7. http://dx.doi.org/10.1016/j.ijadhadh.2017.08.004.

[11] Both JC. Tragfähigkeit von CFK-Metall-Laminaten unter mechanischer und thermischer Belastung: Zugl.: München, Techn. Univ., Diss., 2014. In: ingenieurwissenschaften, München: Dr. Hut; 2014, URL: http://mediatum.ub.tum.de/node?id=1173300.

[12] Liu Q, Ma J, Kang L, Sun G, Li Q. An experimental study on fatigue characteristics of CFRP-steel hybrid laminates. Mater Des 2015;88:643–50. http://dx.doi.org/10.1016/j.matdes.2015.09.024.

[13] Petersen E, Stefaniak D, Hühne C. Experimental investigation of load carrying mechanisms and failure phenomena in the transition zone of locally metal reinforced joining areas. Compos Struct 2017;182(6):79–90. http://dx.doi.org/10.1016/j.compstruct.2017.09.002.

[14] Wu X-t, Zhan L-h, Huang M-h, Zhao X, Wang X, Zhao G-q. Corrosion damage evolution and mechanical properties of carbon fiber reinforced aluminum laminate. J Cent South Univ 2021;28(3):657–68. http://dx.doi.org/10.1007/s11771-021-4635-8.

[15] Klein M, Huelsbusch D, Siddique S, Walther F. Assessment of influence of corrosive environment on fatigue performance of intrinsic CFRP/steel hybrids. Mater Today: Proc 2016;3(9):2861–8. http://dx.doi.org/10.1016/j.matpr.2016.07.005.

[16] Abouhamzeh M. distortions and residual stresses of GLARE induced by manufacturing [Ph.D. thesis], Delft University of Technology; 2016, http://dx.doi.org/10.4233/uuid:1f1b3e5c-72b8-440c-8d98-4b4c82814fb6.

[17] Wiedemann J, Prussak R, Kappel E, Hühne C. In-situ quantification of manufacturing-induced strains in fiber metal laminates with strain gages. Compos Struct 2022;691(1):115967. http://dx.doi.org/10.1016/j.compstruct.2022.115967.

[18] Kim HS, Park SW, Lee DG. Smart cure cycle with cooling and reheating for co-cure bonded steel/carbon epoxy composite hybrid structures for reducing thermal residual stress. Composites A 2006;37(10):1708–21. http://dx.doi.org/10.1016/j.compositesa.2005.09.015.

[19] Khan SU, Alderliesten RC, Benedictus R. Post-stretching induced stress redistribution in fibre metal laminates for increased fatigue crack growth resistance. Compos Sci Technol 2009;69(3–4):396–405. http://dx.doi.org/10.1016/j.compscitech.2008.11.006.

[20] Lin CT, Kao PW, Yang FS. Fatigue behaviour of carbon fibre-reinforced aluminium laminates. Composites 1991;22(2):135–41. http://dx.doi.org/10.1016/0010-4361(91)90672-4.

[21] Mrzljak S, Trautmann M, Wagner G, Walther F. Very high cycle fatigue assessment of thermoplastic-based hybrid fiber metal laminate by using a high-frequency resonant testing system. Int J Fatigue 2024;108361. http://dx.doi.org/10.1016/j.ijfatigue.2024.108361.

[22] Yeh JR. Fatigue crack growth in fiber-metal laminates. Int J Solids Struct 1995;32(14):2063–75. http://dx.doi.org/10.1016/0020-7683(94)00221-H.

[23] Vlot A, van Ingen JW. Delamination resistance of post-stretched fibre metal laminates. J Compos Mater 1998;32(19):1784–805. http://dx.doi.org/10.1177/002199839803201903.

[24] Kim SS, Murayama H, Kageyama K, Uzawa K, Kanai M. Study on the curing process for carbon/epoxy composites to reduce thermal residual stress. Composites A 2012;43(8):1197–202. http://dx.doi.org/10.1016/j.compositesa.2012.02.023.

[25] White SR, Hahn HT. Cure cycle optimization for the reduction of processing-induced residual stresses in composite materials. J Compos Mater 1993;27(14):1352–78. http://dx.doi.org/10.1177/002199839302701402.

[26] Prussak R, Stefaniak D, Kappel E, Hühne C, Sinapius M. Smart cure cycles for fiber metal laminates using embedded fiber bragg grating sensors. Compos Struct 2019;213:252–60. http://dx.doi.org/10.1016/j.compstruct.2019.01.079.

[27] Djokic D, Johnston A, Rogers A, Lee-Sullivan P, Mrad N. Residual stress development during the composite patch bonding process: measurement and modeling. Composites A 2002;33(2):277–88. http://dx.doi.org/10.1016/S1359-835X(01)00083-5.

[28] Kim H-S, Yoo S-H, Chang S-H. In situ monitoring of the strain evolution and curing reaction of composite laminates to reduce the thermal residual stress using FBG sensor and dielectrometry. Composites B 2013;44(1):446–52. http://dx.doi.org/10.1016/j.compositesb.2012.04.021.

[29] Prussak R, Stefaniak D, Hühne C, Sinapius M. Residual stresses in intrinsic UD-CFRP-steel-laminates - experimental determination, identification of sources, effects and modification approaches. In: 20th symposium on composites. Materials science forum, Trans Tech Pubn; 2015, p. 369–76. http://dx.doi.org/10.4028/www.scientific.net/MSF.825-826.369, URL: https://www.scientific.net/MSF.825-826.369.pdf.

[30] Kim HS, Lee DG. Avoidance of fabricational thermal residual stresses in co-cure bonded metal-composite hybrid structures. J Adhesion Sci Technol 2006;20(9):959–79. http://dx.doi.org/10.1163/156856106777657805.

[31] Choi I, Lee DG. Surface modification of carbon fiber/epoxy composites with randomly oriented aramid fiber felt for adhesion strength enhancement. Composites A 2013;48:1–8. http://dx.doi.org/10.1016/j.compositesa.2013.01.003.

[32] Lee KH, Lee DG. Smart cure cycles for the adhesive joint of composite structures at cryogenic temperatures. Compos Struct 2008;86(1–3):37–44. http://dx.doi.org/10.1016/j.compstruct.2008.03.018.

[33] Kim JW, Lee JH, Kim HG, Kim HS, Lee DG. Reduction of residual stresses in thick-walled composite cylinders by smart cure cycle with cooling and reheating. Compos Struct 2006;75(1–4):261–6. http://dx.doi.org/10.1016/j.compstruct.2006.04.029.

[34] Soohyun N, Dongyoung L, Ilbeom C, Dai Gil L. Smart cure cycle for reducing the thermal residual stress of a co-cured E-glass/carbon/epoxy composite structure for a vanadium redox flow battery. Compos Struct 2015;120:107–16. http://dx.doi.org/10.1016/j.compstruct.2014.09.037.

[35] Czapski P, Jakubczak P, Bieniaś J, Urbaniak M, Kubiak T. Influence of autoclaving process on the stability of thin-walled, composite columns with a square cross-section – experimental and numerical studies. Compos Struct 2020;250:112594. http://dx.doi.org/10.1016/j.compstruct.2020.112594.

[36] Droździel M, Podolak P, Czapski P, Zgórniak P, Jakubczak P. Failure analysis of GFRP columns subjected to axial compression manufactured under various curing-process conditions. Compos Struct 2021;262:113342. http://dx.doi.org/10.1016/j.compstruct.2020.113342.

[37] Bienias J, Gliszczynski A, Jakubczak P, Kubiak T, Majerski K. Influence of autoclaving process parameters on the buckling and postbuckling behaviour of thin-walled channel section beams. Thin-Walled Struct 2014;85:262–70. http://dx.doi.org/10.1016/j.tws.2014.09.007.

[38] Kim HS, Park SW, Hwang HY, Lee DG. Effect of the smart cure cycle on the performance of the co-cured aluminum/composite hybrid shaft. Compos Struct 2006;75(1–4):276–88. http://dx.doi.org/10.1016/j.compstruct.2006.04.030.

[39] Khodja M, Fekirini H, Govender G, Bachir Bouiadjra B. Effect of curing cycle on fatigue life of cracked AA7075-T6 aircraft sheet repaired with a boron/epoxy composite patch. Iran J Sci Technol, Trans Mech Eng 2022;46(1):85–97. http://dx.doi.org/10.1007/s40997-020-00400-6.

[40] Hausmann J, Schmidt S. Thermal residual stresses in thermoplastic CFRP-steel laminates: Modification and influence on fatigue life. J Micromech Mol Phys 2021;06(03):49–55. http://dx.doi.org/10.1142/S2424913021430050.

[41] Laliberté J, Mahendran M, Djokic D, Li C, Kratz J. Effect of process-induced residual stresses on mechanical properties and fatigue crack initiation in fibre metal laminates. In: Lazzeri L, editor. ICAF 2007 : Durability and damage tolerance of aircraft structures: Metals vs composites; Proceedings of the 24th symposium of the International Committee on Aeronautical Fatigue. Pisa: Pacini Ed.; 2007, p. 576–92.

[42] Barth T, Wiedemann J, Roloff T, Behrens T, Rauter N, Hühne C, et al. Experimental determination of dispersion diagrams over large frequency ranges for guided ultrasonic waves in fiber metal laminates. Smart Mater Struct 2023;32(8):085011. http://dx.doi.org/10.1088/1361-665X/ace0ea.

[43] Johnston AA. An integrated model of the development of process-induced deformation in autoclave processing of composite structures [Ph.D. thesis], Vancouver, Kanada: University of British Columbia; 1997, http://dx.doi.org/10.14288/1.0088805.

[44] Wiedemann J, Schmidt J-UR, Hühne C. Applicability of asymmetric specimens for residual stress evaluation in fiber metal laminates. J Compos Sci 2022;6(11):329. http://dx.doi.org/10.3390/jcs6110329.

[45] National Institute for Aviation Research - Wichita State University. Hexcel 8552 AS4 unidirectional prepreg at 190 gsm & 35% RC: Qualification material property data report. 2011, URL: https://www.wichita.edu/research/NIAR/Research/hexcel-8552/AS4-Unitape-2.pdf.

[46] Hexcel Corporation. Product data sheet HexPly 8552. 2020, URL: https://www.hexcel.com/user_area/content_media/raw/HexPly_8552_eu_DataSheet.pdf.

[47] Garstka T. separation of process induced distortions in curved composite laminates [Ph.D. thesis], Bristol: The University of Bristol; 2005.

[48] Hörberg E, Nyman T, Åkermo M, Hallström S. Thickness effect on spring-in of prepreg composite L-profiles – An experimental study. Compos Struct 2019;209(8):499–507. http://dx.doi.org/10.1016/j.compstruct.2018.10.090.

[49] Kappel E. On thermal-expansion properties of more-orthotropic prepreg laminates with and without interleaf layers. Composites C 2020;3(17):100059. http://dx.doi.org/10.1016/j.jcomc.2020.100059.

[50] Koch SF, Barfuss D, Bobbert M, Groß L, Grützner R, Riemer M, et al. Intrinsic hybrid composites for lightweight structures: New process chain approaches. Adv Mater Res 2016;1140:239–46. http://dx.doi.org/10.4028/www.scientific.net/AMR.1140.239.

[51] 3M Aerospace and Commercial Transportation Division. 3M™ surface pre-treatment AC-130-2. 2015, URL: https://multimedia.3~m.com/mws/media/1063834O/3m-surface-pre-treatment-ac-130-2-application-guide.pdf.

[52] Viandier A, Stefaniak D, Hühne C, Sinapius M. Hybridisation as an efficient joining, electrochemical corrosion study as a need. Galvanotechnik 2017;2017(1). http://dx.doi.org/10.12850/ISSN2196-0267.JEPT5763.

[53] DIN Deutsches Institut für Normung eV. Plastics - determination of tensile properties - part 5: Test conditions for unidirectional fibre-reinforced plastic composites (iso 527-5:2021). 2022.

[54] Koord J, Stüven J-L, Petersen E, Völkerink O, Hühne C. Investigation of exact analytical solutions for circular notched composite laminates under tensile loading. Compos Struct 2020;243:112180. http://dx.doi.org/10.1016/j.compstruct.2020.112180.

[55] Koord J. design methodology for highly loaded composite bolted joints with local metal hybridization at low temperature: DLR-forschungsbericht - DLR-FB-2024-11 [Ph.D. thesis], Braunschweig: Technische Universität Carolo-Wilhelmina zu Braunschweig; 2024, http://dx.doi.org/10.57676/mzxc-3158.

[56] Nettles AT. Basic mechanics of laminated composite plates: technical report: nasa-rp-1351. 1994, URL: https://ntrs.nasa.gov/citations/19950009349.

[57] Wu T, Degener S, Tinkloh S, Liehr A, Zinn W, Nobre JP, et al. Characterization of residual stresses in fiber metal laminate interfaces – A combined approach applying hole-drilling method and energy-dispersive X-ray diffraction. Compos Struct 2022;299:116071. http://dx.doi.org/10.1016/j.compstruct.2022.116071.

[58] Lekhnitskii SG. Anisotropic plates: Translated from the second Russian edition by S.W. Tsai and T. Cheron. New York: Gordon and Breach; 1968.

[59] Savin GN. Stress distribution around holes. Nasa Technical Translation; 1968.

[60] Koord J, Stüven J-L, Völkerink O, Petersen E, Hühne C. Investigation of exact analytical solutions for composite laminates under pin-bearing loading. Compos Struct 2022;292:115605. http://dx.doi.org/10.1016/j.compstruct.2022.115605.

[61] Soutis C, Filiou C. Stress distributions around holes in composite laminates subjected to biaxial loading. Appl Compos Mater 1998;5(6):365–78. http://dx.doi.org/10.1023/a:1008837715030.

[62] Mrzljak S, Trautmann M, Wagner G, Walther F. Influence of aluminum surface treatment on tensile and fatigue behavior of thermoplastic-based hybrid laminates. Materials (Basel, Switzerland) 2020;13(14). http://dx.doi.org/10.3390/ma13143080.

[63] Takamatsu T, Matsumura T, Ogura N, Shimokawa T, Kakuta Y. Fatigue crack growth properties of a GLARE3-5/4 fiber/metal laminate. Eng Fract Mech 1999;63(3):253–72. http://dx.doi.org/10.1016/S0013-7944(99)00021-1.

[64] Burgers A, Kempen PD. Automatic crack length measurements by the electrical potential drop method with computer control: Report LR-309. 1980, URL: http://resolver.tudelft.nl/uuid:92d25f8b-960a-4192-865a-a7ea3ad0d377.

[65] Alderliesten RC. Fatigue crack propagation and delamination growth in glare [Ph.D. thesis], Netherlands: Technische Universiteit Delft; 2005.

[66] Mandell JF, Samborsky DD, Wang L, Wahl NK. New fatigue data for wind turbine blade materials. In: ASME 2003 wind energy symposium. ASMEDC; 2003, p. 167–79. http://dx.doi.org/10.1115/WIND2003-692.